Geosci. Model Dev. Discuss., doi:10.5194/gmd-2016-176, 2016
Manuscript under review for journal Geosci. Model Dev.
Published: 13 September 2016

Geoscientific Model Development Discussions
Open Access
EGU

An axisymmetric non-hydrostatic model for double-diffusive water systems

Koen Hilgersom[1], Marcel Zijlema[2], and Nick van de Giesen[1]

[1]Water Resources Section, Faculty of Civil Engineering and Geosciences, Delft University of Technology, Delft, P.O. Box 5048, 2600 GA, The Netherlands
[2]Environmental Fluid Mechanics Section, Faculty of Civil Engineering and Geosciences, Delft University of Technology, Delft, P.O. Box 5048, 2600 GA, The Netherlands

Correspondence to: Koen Hilgersom (k.p.hilgersom@tudelft.nl)

Abstract. The three-dimensional (3-D) modelling of water systems involving double-diffusive processes is challenging due to the large computation times required to solve the flow and transport of constituents. In systems that approach axisymmetry around a central location, computation times can be reduced by applying a quasi 3-D axisymmetric model setup. This article applies the Navier-Stokes equations described in cylindrical coordinates, and integrates them to guarantee mass and momentum conservation. The discretized equations are presented in a way that a Cartesian finite volume model can be easily extended to this quasi 3-D framework, which is demonstrated by the implementation into a non-hydrostatic free-surface flow model. This model employs temperature and salinity dependent densities, molecular diffusivities, and kinematic viscosity. Four qualitative case studies demonstrate a good behaviour with respect to expected density and diffusivity driven flow and stratification in shallow water bodies. A fifth case study involves a new validation method that quantifies the radial expansion of a dense water layer developing from a central inflow at the bottom of a shallow water body.

1 Introduction

Over the past decades, numerical salt and heat transport models have increased their capability to capture patterns of double-diffusion on scales varying from laboratory set-ups to the ocean (Yoshida and Nagashima, 2003; Kunze, 2003). Despite the advance in computation power and parallel computing, the requirement of dense grids for the three-dimensional (3-D) modelling of salt and heat transport often yields unacceptable computation times. In this article, we present a framework for a

Geosci. Model Dev. Discuss., doi:10.5194/gmd-2016-176, 2016
Manuscript under review for journal Geosci. Model Dev.
Published: 13 September 2016

quasi 3-D finite volume approach that allows free-surface flow modelling in an axisymmetric grid, under the influence of double-diffusion.

Kunze (2003) stresses that numerical and analytical methods to model double-diffusion often only apply at specific scales. For example in oceans, internal wave-shear and strain enhance salt-finger growth, leading to higher salt and heat fluxes over stratified interfaces. Traxler et al. (2011) addresses the issue of scale by describing four modes of instability in salt-fingering systems, which play a role on different scales. Yoshida and Nagashima (2003) have shown that 2-D numerical models are already well able to simulate small-scale processes in laboratory set-ups.

Numerical modelling studies of double-diffusive processes often calculate interfaces and salt and heat fluxes at oceanic scale (Stommel and Fedorov, 1967; Stern, 1967; Ruddick and Gargett, 2003; Kelley et al., 2003; Kunze, 2003; Kimura et al., 2011). This can be explained by the ubiquity of these systems in oceans (Huppert and Turner, 1981), and by the potential of oceanic thermohaline stratification as an energy source (Stommel et al., 1956; Vega, 2002). More recently, modelling of these phenomena in smaller-scale water bodies has started to be developed. For example, double-diffusive processes like thermohaline staircasing have been successfully modelled in lakes (Schmid et al., 2003), although these systems are generally modelled with analytical or empirical formulations (Kelley et al., 2003; Schmid et al., 2004; Arnon et al., 2014). Other known numerical modelling studies consider double-diffusive convection in monitoring wells (Berthold and Börner, 2008), and the collection of thermal energy in solar ponds (Cathcart and Wheaton, 1987; Giestas et al., 2009; Suárez et al., 2010, 2014). However, modelling these complex physical processes in shallow waters still imposes a major scientific and computational challenge (Dias and Lopes, 2006).

Axisymmetric CFD models are applied in a wide variety of fields. Examples of applications include the modelling of flow of gas past a gravitating body in astronomy (Shima et al., 1985), radiative heat transfer in cylindrical enclosures (Menguc and Viskanta, 1986), the heating of air flowing through a combustion burner (Galletti et al., 2007), and acoustic axisymmetric waves in elastic media (Schubert et al., 1998). The similarity between these examples is that a model calculating in two spatial dimensions models 3-D processes due to axisymmetry. In geohydrology, axisymmetric models are often applied for groundwater flow around injection and abstraction wells (Bennett et al., 1990). Groundwater modelling software often offers code extensions that adjust several input parameters to allow such modelling approaches (Reilly and Harbaugh, 1993; Langevin, 2008).

In some cases, axisymmetric grid set-ups can also be preferential for hydrodynamic surface water models. Examples of such cases are close-to-circular water bodies with uniform boundaries, and the flow around a central point: for example, a local inflow from a pipe or groundwater seepage (De Louw et al., 2013).

This article derives a framework for an axisymmetric free-surface flow model, which is implemented in SWASH. SWASH is an open source non-hydrostatic modelling code for the simulation of coastal flows including baroclinic forcing (SWASH source code, 2010). It is suitable for the simula-

Geosci. Model Dev. Discuss., doi:10.5194/gmd-2016-176, 2016
Manuscript under review for journal Geosci. Model Dev.
Published: 13 September 2016

Geoscientific Model Development Discussions
Open Access
EGU

tion of flows and transport in varying density fields, because 1) the momentum and mass conservative grid setup allows accurate modelling of transport processes, and 2) the non-hydrostatic pressure terms aid the simulation of flows in fields with large density variations. Another major advantage of SWASH is the flexible and easily extendible code, which can be applied for free under the GNU GPL license. Other properties of SWASH are the opportunity to apply terrain-following σ-layers for the definition of cell depths and the user-friendly pre- and post-processing.

In the course of our study of localized saline water seepage in Dutch polders, we developed an axi-symmetric variation of SWASH. Here, we present the resulting numerical framework to extend a 2-D finite volume model into a quasi 3-D model by adding few terms to the solution of the governing Navier-Stokes and transport equations. These terms are implemented in the SWASH code. The model code is further extended with a new transport module calculating salt and heat transfer. Although the model generally calculates with a mesh size that is larger than the size required to solve small-scale double-diffusive instabilities, the aim is to allow the model to approximate interface locations and salt and heat fluxes. The model code does not require the calibration of model parameters. The functioning of the code is validated with case studies involving different salinity and temperature gradients.

2 Method

2.1 Governing equations

The governing equations in this study are the Navier-Stokes equations for the flow of an incompressible fluid, derived in cylindrical coordinates (r, θ, z) (Batchelor, 1967). Due to point symmetry, the gradients in tangential direction (θ) are set to zero, which leaves the solution of the equations in one horizontal and one vertical dimension (i.e., 2-DV):

$$\frac{1}{r}\frac{\partial ur}{\partial r} + \frac{\partial w}{\partial z} = 0 \tag{1}$$

$$\frac{\partial u}{\partial t} + \frac{\partial uu}{\partial r} + \frac{\partial wu}{\partial z} = -\frac{1}{\rho}\frac{\partial p}{\partial r} + \left(\frac{1}{r}\frac{\partial}{\partial r}\left(\nu_h r \frac{\partial u}{\partial r}\right) - \frac{\nu_h u}{r^2} + \frac{\partial}{\partial z}\left(\nu_v \frac{\partial u}{\partial z}\right)\right) \tag{2}$$

$$\frac{\partial w}{\partial t} + \frac{\partial uw}{\partial r} + \frac{\partial ww}{\partial z} = -\frac{1}{\rho}\frac{\partial p}{\partial z} + \frac{1}{r}\frac{\partial}{\partial r}\left(\nu_h r \frac{\partial w}{\partial r}\right) + \frac{\partial}{\partial z}\left(\nu_v \frac{\partial w}{\partial z}\right) - g \tag{3}$$

In these equations, r represents the horizontal axis in radial direction and z the vertical axis, with u and w the velocities along these axes, respectively. The density ρ is calculated from the local temperature and salinity states by the updated Eckart formula (Eckart, 1958; Wright, 1997), which is based on the UNESCO IES80 formula (Unesco, 1981). For the calculations in this article,

Geosci. Model Dev. Discuss., doi:10.5194/gmd-2016-176, 2016
Manuscript under review for journal Geosci. Model Dev.
Published: 13 September 2016

Geoscientific Model Development Discussions
Open Access
EGU

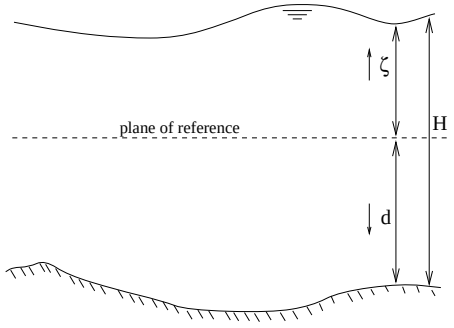

Figure 1. Definition of the free surface level ζ and the bottom level d (Zijlema and Stelling, 2005).

the horizontal kinematic viscosity ν_h is set uniform to its molecular value (~ 10^{-6} $\mathrm{m^2 s^{-1}}$). The non-uniform vertical viscosity ν_v includes the local eddy viscosity, as calculated by the standard k-ϵ model (Launder and Spalding, 1974). The pressure terms are split into hydrostatic and hydrodynamic terms, according to Casulli and Stelling (1998):

$$\frac{1}{\rho}\frac{\partial p}{\partial r} = \frac{g}{\rho}\frac{\partial \int_{z'=z}^{\zeta} \rho(r,z',t)\,dz'}{\partial r} + \frac{\partial q}{\partial r} \tag{4}$$

$$\frac{1}{\rho}\frac{\partial p}{\partial z} + g \equiv \frac{\partial q}{\partial z} \tag{5}$$

where q denotes the hydrodynamic pressure component and ζ the local free surface level relative to the reference plane (Fig. 1). Horizontal variations in atmospheric pressure are neglected. The first right-hand side term of Equation 4 is split into baroclinic and barotropic components when the equations are integrated over the cell depth in Section 2.3. In the vertical, the baroclinic pressure gradient and the gravitational acceleration cancel each other out, leaving the hydrodynamic pressure gradient (Equation 5).

The free surface is calculated according to Zijlema and Stelling (2008), by integrating Eq. 1 over the depth of the water column:

$$\frac{\partial \zeta}{\partial t} + \frac{\partial Q}{\partial t} = 0, Q \equiv UH = \int_{-d}^{\zeta} u dz \tag{6}$$

where U is the depth-averaged velocity, and d is the local bottom depth (Fig. 1).

Transport of mass and heat is calculated with the convection-diffusion equation:

$$\frac{\partial c}{\partial t} + \frac{1}{r}\frac{\partial ruc}{\partial r} + \frac{\partial wc}{\partial z} = \frac{1}{r}\frac{\partial}{\partial r}\left(D_h r \frac{\partial c}{\partial r}\right) + \frac{\partial}{\partial z}\left(D_v \frac{\partial c}{\partial r}\right) \tag{7}$$

Geosci. Model Dev. Discuss., doi:10.5194/gmd-2016-176, 2016
Manuscript under review for journal Geosci. Model Dev.
Published: 13 September 2016

Geoscientific Model Development Discussions
Open Access
EGU

where the concentration c represents either the salinity S or temperature T.

To account for turbulent diffusion, D_h and D_v are calculated by adding the molecular diffusivities and turbulent diffusivities: $D = D_{mol} + D_{turb}$. The turbulent diffusivities are calculated by dividing the eddy viscosity ν_{turb} by the turbulent Prandtl number ($Pr = 0.85$) in the case of heat transport, or by the turbulent Schmidt number ($Sc = 0.7$) in the case of salt transport:

$$D_{turb;T} = \frac{\nu_{turb}}{Pr} = \frac{\nu_{turb}}{0.85} \tag{8}$$

$$D_{turb;S} = \frac{\nu_{turb}}{Sc} = \frac{\nu_{turb}}{0.7} \tag{9}$$

with $D_{turb;T}$ and $D_{turb;S}$ being the thermal and solutal turbulent diffusivities in $\mathrm{m^2 s^{-1}}$, respectively.

In non-turbulent thermohaline systems, stability largely depends on density gradients and molecular heat and salt diffusion rates, which in turn are highly dependent on temperature and salinity. The heat and salt diffusivities are related to temperature T ($^\circ$C) and salinity S ($\mathrm{weight} - \%$) by a quadratic regression on data presented in the International Critical Tables of Numerical Data, Physics, Chemistry and Technology (Washburn and West, 1933):

$$D_{mol;T} = 1.31721 + 4.26657 \cdot 10^{-3} \cdot T - 1.09237 \cdot 10^{-6} \cdot T^2 + 1.74051 \cdot 10^{-2} \cdot S - 3.17759 \cdot 10^{-4} \cdot S^2 \tag{10}$$

$$D_{mol;S} = 7.66025 + 2.33023 \cdot 10^{-1} \cdot T + 3.21974 \cdot 10^{-3} \cdot T^2 - 2.18290 \cdot 10^{-1} \cdot S + 1.34431 \cdot 10^{-2} \cdot S^2 \tag{11}$$

2.2 Boundary conditions

At the free surface, we assume no wind and $q|_{z=\zeta} = 0$. At the bottom boundary, the vertical velocity is calculated by imposing the kinematic condition $w|_{z=-d} = -u\partial d/\partial r$. The presented case studies (Section 3) include a local seepage inflow at the bottom boundary, for which the seepage velocity is added to the kinematic condition. For horizontal momentum, friction is imposed through the Chezy coefficient C:

$$\nu_v \frac{\partial u}{\partial z}\bigg|_{z=-d} = \frac{g}{C^2} \cdot |U| \cdot u_{k=1} \tag{12}$$

with $u_{k=1}$ is the horizontal velocity in the bottom cell (Figure 2).

Geosci. Model Dev. Discuss., doi:10.5194/gmd-2016-176, 2016
Manuscript under review for journal Geosci. Model Dev.
Published: 13 September 2016

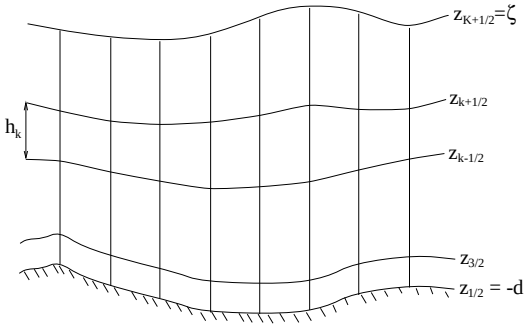

Figure 2. Vertical grid definition (sigma layers) (Zijlema and Stelling, 2005)

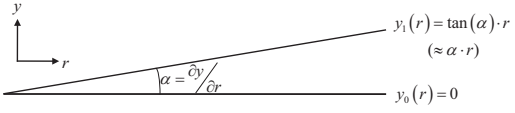

Figure 3. Axis definition

A special case is the inner boundary, where symmetry occurs: for all variables, the gradient is set to zero, except for horizontal momentum: $u|_{r=0} = 0$. For the presented case studies, we define a Dirichlet boundary condition for u momentum at the outer boundary, where the total outflow is equated to the instantaneous seepage inflow.

For the transport equation, a homogeneous Neumann boundary condition is defined at each boundary ($\frac{\partial c}{\partial r} = 0$ and $\frac{\partial c}{\partial z} = 0$), except at a defined seepage inflow of known temperature and salt concentration, where a Dirichlet boundary condition is imposed.

2.3 Numerical framework and implementation

The physical domain is discretized with a fixed cell width in radial direction. The width of the cells in tangential direction increases by a fixed angle α, which allows us to consider the horizontal grid as a pie slice (Figure 3). In the model, α could be assigned any value (i.e., also 2π for a completely circular grid). However, to allow a simple presentation of the integration step in this subsection, we consider α as a small angle.

For the vertical grid, sigma layering is employed, although part of the layers can be defined by a fixed cell depth (Figure 2). A classical staggered grid is applied with velocities defined at the cell boundaries and the other states in the cell centre.

For reasons of momentum and mass conservation, Zijlema and Stelling (2005) integrated the governing equations over the cell depth using the Leibniz integral rule (Appendix A). In our case, the cell width in tangential direction varies as well. Therefore, the equations are integrated over the

Geosci. Model Dev. Discuss., doi:10.5194/gmd-2016-176, 2016
Manuscript under review for journal Geosci. Model Dev.
Published: 13 September 2016

Geoscientific Model Development Discussions
Open Access
EGU

cell depth and the width in tangential direction, which is in this case defined as the y-dimension. For the continuity equation, this yields (cf. Figures 2 and 3):

$$\int_{z_{k-\frac{1}{2}}}^{z_{k+\frac{1}{2}}} \int_{y_0}^{y_1} \left(\frac{1}{r} \frac{\partial ur}{\partial r} + \frac{\partial w}{\partial z} \right) dy dz = \frac{\partial \phi_k y_1}{\partial r} + y_1 \omega_{k+\frac{1}{2}} - y_1 \omega_{k-\frac{1}{2}} + y_1 \frac{\partial h_k}{\partial t} = 0 \tag{13}$$

with $\phi_k = u_k \cdot h_k$ is the cell depth integrated velocity.

The momentum equations and the transport equation are integrated in a similar fashion:

$$\begin{aligned} &\overline{y_1}^r \frac{\partial u_k \overline{h_k}^r}{\partial t} + \frac{\partial \overline{\phi_k}^r \hat{u}_k \overline{y_1}^r}{\partial r} + \overrightarrow{y_1} \hat{u}_{k+\frac{1}{2}} \overline{\omega_{k+\frac{1}{2}}}^r - \overrightarrow{y_1} \hat{u}_{k-\frac{1}{2}} \overline{\omega_{k-\frac{1}{2}}}^r - \boxed{\alpha \phi_k u_k} + g \overline{h_k}^r \overline{y_1}^r \frac{\partial \zeta}{\partial r} + \\ &\frac{\partial q_k h_k y_1}{\partial r} - \overline{y_1}^r \overline{q}^{rz} \frac{\partial z_{i+\frac{1}{2},k+\frac{1}{2}}}{\partial r} + \overline{y_1}^r \overline{q}^{rz} \frac{\partial z_{i+\frac{1}{2},k-\frac{1}{2}}}{\partial r} - \boxed{\alpha \overline{h_k}^r \overline{q_k}^r} + \overline{y_1}^r \frac{g}{\overline{\rho_k}} \frac{\partial \overline{\rho_k}}{\partial r} \frac{\left(\overline{h_k}^r\right)^2}{2} + \\ &\frac{g \overline{h_k}^r \overline{y_1}^r}{\overline{\rho_k}} \sum_{j=1}^{k-1} \left(\overline{h_j}^r \frac{\partial \overline{\rho_j}}{\partial r} + (\overline{\rho_j} - \overline{\rho_k}) \frac{\partial h_j}{\partial r} \right) - \frac{\partial}{\partial r} \nu_h h_k y_1 \frac{\partial \overline{u_k}}{\partial r} + \\ &\boxed{\alpha h_k u_k \frac{\nu_h}{r}} - \overline{y_1}^r \left[\nu_v \frac{\partial u}{\partial z} \right]_{k-\frac{1}{2}}^{k+\frac{1}{2}} = 0 \end{aligned} \tag{14}$$

$$\begin{aligned} &y_1 \frac{\partial w_{k+\frac{1}{2}} \overline{h_{k+\frac{1}{2}}}^z}{\partial t} + \frac{\partial \hat{w}_{k+\frac{1}{2}} \overline{\phi_{k+\frac{1}{2}}}^z y_1}{\partial r} - \boxed{\alpha \overline{\phi_{k+\frac{1}{2}}}^{rz} w_{k+\frac{1}{2}}} + y_1 \hat{w}_{k+1} \overline{\omega_{k+1}}^z - y_1 \hat{w}_k \overline{\omega_k}^z + \\ &y_1 q_{k+1} - y_1 q_k - \frac{\partial}{\partial r} \nu_h \overline{y_1}^r \overline{h_{k+\frac{1}{2}}}^{rz} \frac{\partial \overline{w}}{\partial r} - y_1 \left[\nu_v \frac{\partial w}{\partial z} \right]_k^{k+1} = 0 \end{aligned} \tag{15}$$

$$\begin{aligned} &y_1 \frac{\partial c_k h_k}{\partial t} + \frac{\partial \phi_k c_k y_1}{\partial r} + y_1 \omega_{k+\frac{1}{2}} \hat{c}_{k+\frac{1}{2}} - y_1 \omega_{k-\frac{1}{2}} \hat{c}_{k-\frac{1}{2}} - \frac{\partial}{\partial r'} \left\{ D_h \overline{y_1}^r \overline{h_k}^r \frac{\partial c}{\partial r'} \right\} - \\ &y_1 \left[D_v \frac{\partial c}{\partial z'} \right]_{z_{k-\frac{1}{2}}}^{z_{k+\frac{1}{2}}} + \frac{\partial}{\partial r'} \left\{ D_h \overline{y_1}^r \overline{h_k}^r \frac{\partial \overline{c_k}^r}{\partial z'} \frac{\partial \overline{z}^z}{\partial r'} \right\} + y_1 \left[D_h \frac{\partial z_k}{\partial r} \frac{\partial c}{\partial r'} \right]_{z_{k-\frac{1}{2}}}^{z_{k+\frac{1}{2}}} - \\ &y_1 \left[D_h \left(\frac{\partial z}{\partial r} \right)^2 \frac{\partial c}{\partial z'} \right]_{z_{k-\frac{1}{2}}}^{z_{k+\frac{1}{2}}} = 0 \end{aligned} \tag{16}$$

where overlined variables denote spatially averaged values for these variables in r or z directions, and arrows denote the use of values from downstream cells. The boxes mark the *alpha terms*, which mark the additional angular terms compared to the 2-DV solutions for the momentum equations in Cartesian coordinates. In the integrated transport equation (Equation 16), the latter three terms on the left-hand side are the so-called anti-creepage terms, which should be incorporated for the calculation of transport when large gradients in water depth occur.

Since u and w are the primitive variables in the momentum equations, and not uh and wh as in Equations 14 and 15, we further rewrite the momentum equations according to Zijlema and Stelling

Geosci. Model Dev. Discuss., doi:10.5194/gmd-2016-176, 2016
Manuscript under review for journal Geosci. Model Dev.
Published: 13 September 2016

Geoscientific Model Development Discussions

(2008). In order to do this for the u momentum equation, we first spatially discretize the continuity equation in point $i+\frac{1}{2}$:

$$\overline{y_{1;i+\frac{1}{2}}}^{r}\frac{\partial \overline{h}^{r}_{i+\frac{1}{2},k}}{\partial t}+\frac{y_{1;i+1}\overline{\phi}^{r}_{i+1,k}-y_{1;i}\overline{\phi}^{r}_{i,k}}{\Delta r}+\overline{y}^{r}_{1;i+\frac{1}{2}}\left(\overline{\omega}^{r}_{i+\frac{1}{2},k+\frac{1}{2}}-\overline{\omega}^{r}_{i+\frac{1}{2},k-\frac{1}{2}}\right)=0 \tag{17}$$

We then spatially discretize the u momentum equation and expand $\partial u_k h_k/\partial t$ to $h_k \partial u_k/\partial t + u_k \partial h_k/\partial t$. The latter term falls out by subtracting Equation 17 multiplied by u_k from Equation 14:

$$\begin{aligned}
&\overline{y}^{r}_{1;i+\frac{1}{2}}\overline{h}^{r}_{i+\frac{1}{2},k}\frac{\partial u_{i+\frac{1}{2},k}}{\partial t}+\frac{\overline{\phi}^{r}_{i+1,k}\overline{y}^{r}_{1;i+1}\left(\hat{u}_{i+1,k}-u_{i+\frac{1}{2},k}\right)-\overline{\phi}^{r}_{i+1,k}\overline{y}^{r}_{1;i+1}\left(\hat{u}_{i+1,k}-u_{i+\frac{1}{2},k}\right)}{\Delta r}+\\
&\overrightarrow{y}_{1;i+\frac{1}{2}}\hat{u}_{i+\frac{1}{2},k+\frac{1}{2}}\overline{\omega}^{r}_{i+\frac{1}{2},k+\frac{1}{2}}-\overrightarrow{y}_{1;i+\frac{1}{2}}\hat{u}_{i+\frac{1}{2},k-\frac{1}{2}}\overline{\omega}^{r}_{i+\frac{1}{2},k-\frac{1}{2}}-\boxed{\alpha\phi_{i+\frac{1}{2},k}u_{i+\frac{1}{2},k}}+\\
&g\overline{h}^{r}_{i+\frac{1}{2},k}\overline{y}^{r}_{1;i+\frac{1}{2}}\frac{\zeta_{i+1}-\zeta_i}{\Delta r}+\frac{q_{i+1,k}h_{i+1,k}y_{1;i+1}-q_{i,k}h_{i,k}y_{1;i}}{\Delta r}-\\
&\overline{y}^{r}_{1;i+\frac{1}{2}}\overline{q}^{rz}_{i+\frac{1}{2},k+\frac{1}{2}}\frac{z_{i+1,k+\frac{1}{2}}-z_{i,k+\frac{1}{2}}}{\Delta r}+\overline{y}^{r}_{1;i+\frac{1}{2}}\overline{q}^{rz}_{i+\frac{1}{2},k-\frac{1}{2}}\frac{z_{i+1,k-\frac{1}{2}}-z_{i,k-\frac{1}{2}}}{\Delta r}-\\
&\boxed{\alpha\overline{h}^{r}_{i+\frac{1}{2},k}\overline{q}^{r}_{i+\frac{1}{2},k}}+\overline{y}^{r}_{1;i+\frac{1}{2}}\frac{g}{\overline{\rho}^{r}_{i+\frac{1}{2},k}}\frac{\rho_{i+1,k}-\rho_{i,k}}{\Delta r}\frac{\left(\overline{h}^{r}_{i+\frac{1}{2},k}\right)^2}{2}+\\
&\frac{g\overline{h}^{r}_{i+\frac{1}{2},k}\overline{y}^{r}_{1;i+\frac{1}{2}}}{\overline{\rho}^{r}_{i+\frac{1}{2},k}}\sum_{j=1}^{k-1}\left(\overline{h}^{r}_{i+\frac{1}{2},j}\frac{\rho_{i+1,j}-\rho_{i,j}}{\Delta r}+\left(\overline{\rho}^{r}_{i+\frac{1}{2},j}-\overline{\rho}^{r}_{i+\frac{1}{2},k}\right)\frac{h_{i+1,j}-h_{i,j}}{\Delta r}\right)-\\
&\frac{\nu_h}{\Delta r}\left(h_{i+1,k}y_{1;i+1}\frac{u_{i+\frac{3}{2},k}-u_{i+\frac{1}{2},k}}{\Delta r}-h_{i,k}y_{1;i}\frac{u_{i+\frac{1}{2},k}-u_{i-\frac{1}{2},k}}{\Delta r}\right)+\boxed{\alpha\overline{h}^{r}_{i+\frac{1}{2},k}u_{i+\frac{1}{2},k}\frac{\nu_h}{r_{i+\frac{1}{2}}}}-\\
&\overline{y_{1;i+\frac{1}{2}}}^{r}\left(\nu_{v;i+\frac{1}{2},k+\frac{1}{2}}\frac{u_{i+\frac{1}{2},k+1}-u_{i+\frac{1}{2},k}}{\overline{h}^{rz}_{i+\frac{1}{2},k+\frac{1}{2}}}-\nu_{v;i+\frac{1}{2},k-\frac{1}{2}}\frac{u_{i+\frac{1}{2},k}-u_{i+\frac{1}{2},k-1}}{\overline{h}^{rz}_{i+\frac{1}{2},k-\frac{1}{2}}}\right)=0
\end{aligned} \tag{18}$$

Again, the alpha terms are marked with boxes. Another addition compared to the Cartesian 2-DV solution are the y-factors throughout the equation, which serve as width compensation factors. For w momentum, a similar procedure is applied.

The governing equations are spatially discretized with a central differences approach, except for the advective terms. The advective terms are discretized with higher-order flux limiters (Fringer et al., 2005), namely MINMOD flux limiters in the case of the momentum equations, and MUSCL flux limiters in the case of the transport equation.

The horizontal time integration of the momentum and transport equations is Euler explicit. The horizontal advective terms in the momentum equations are solved with the predictor-corrector scheme of MacCormack (Hirsch, 1988). The vertical time integration is semi-implicit, applying the θ-scheme. The global continuity equation (Equation 6) and barotropic forcing are solved semi-implicitly (Casulli and Cheng, 1992). The case studies (Section 2.4) apply an implicitness factor $\theta = 1$ (i.e., the Euler implicit scheme) for the vertical momentum and transport equations, the global continuity

Geosci. Model Dev. Discuss., doi:10.5194/gmd-2016-176, 2016
Manuscript under review for journal Geosci. Model Dev.
Published: 13 September 2016

Geoscientific Model Development Discussions
Open Access
EGU

equation, and the barotropic forcing. The non-hydrostatic pressure is standard solved with the Euler implicit scheme. The complete discretizations are shown in Appendix B.

The numerical framework largely follows the SWASH solution procedure (Zijlema et al., 2011). The code was expanded by adding the alpha terms and factors accounting for the varying cell width in tangential direction. The density and transport calculation modules were replaced by new modules based on the selected density equation (Wright, 1997), and the presented diffusivity equations.

2.4 Verification and validation

This article validates the model qualitatively and quantitatively. The qualitative validation is based on the expected stability of a dual layered double-diffusive system. The stability of a double-diffusive system is often expressed by its Turner angle Tu (Ruddick, 1983):

$$Tu = \arctan\left(\frac{N_T^2 - N_S^2}{N_T^2 + N_S^2}\right) \tag{19}$$

where $N_T^2 = -g \cdot \alpha_V \cdot \partial T/\partial z$, $N_S^2 = g \cdot \beta_V \cdot \partial S/\partial z$, α_V and β_V are the volumetric expansion coefficients for temperature and salinity, respectively, and the z-axis is in downward direction. A stable system occurs for $|Tu| < 45^{\circ}$, whereas $|Tu| > 90^{\circ}$ yields a gravitationally unstable system. Double-diffusive convection occurs for $-90^{\circ} < Tu < -45^{\circ}$, and salt-fingering for $45^{\circ} < Tu < 90^{\circ}$.

The expansion coefficients α_V and β_V are dependent on temperature and salinity itself, and are calculated for the average salinity and temperature on the interface. The expansion coefficients are derived from a linear regression to the density derivatives to temperature and salinity, where the density is calculated according to Wright (1997):

$$\alpha_V(T,S) = -2.285097\cdot10^{-5} + 1.324876\cdot10^{-5}\cdot T - 9.288537\cdot10^{-8}\cdot T^2 + 1.563353\cdot10^{-6}\cdot S \tag{20}$$

$$\beta_V(T,S) = 7.998742\cdot10^{-4} - 2.774404\cdot10^{-6}\cdot T + 3.188185\cdot10^{-8}\cdot T^2 - 4.151510\cdot10^{-7}\cdot S \tag{21}$$

The Turner angles are calculated for several case studies by taking the average of the expansion coefficients for the layers above and below the interface (Table 1). Cases 1 and 2 concern a system with two layers of equal depth, where a warm and salt water layer is overlying a cold and fresh water layer. Based on the Turner angle, salt-fingers are expected to occur. These salt-fingers are induced by applying a few very small perturbations of order 10^{-6} °C throughout the temperature field. Case 1 has a larger density ratio $R_\rho = -N_T^2/N_S^2$ than Case 2, yielding a lower salt flux over the interface (Kunze, 2003). In Case 3 and 4, a dual-layered system is built up by a central inflow through the bottom with an outer radius of 0.25 m. The inflow velocity w_{in} is built up linearly over the first 10 minutes to prevent a sudden pressure wave at $t = 0$. The average water level is kept constant by an

Geosci. Model Dev. Discuss., doi:10.5194/gmd-2016-176, 2016
Manuscript under review for journal Geosci. Model Dev.
Published: 13 September 2016

Geoscientific Model Development Discussions
Open Access
EGU

Table 1. The dimensions, properties, and consequent stability parameters applied in the case studies. *Up* and *Down* refer to the upper and lower layer of the dual layered system (in Case 3 to 5, the lower temperatures and salinities are properties of the central inflow).

Case	Dimension (m)		T (°C)		S (weight $-$ ‰)		w_{in} (ms^{-1})	Tu (°)	R_ρ $-$
	Depth	Radial	Up	Down	Up	Down			
1	0.7	2.0	20	10	1	0	-	71.2	2.04
2	0.7	2.0	20	15	1	0	-	85.0	1.19
3	0.5	1.5	20	25	1	3	$1 \cdot 10^{-3}$	-85.5	0.77
4	0.5	1.5	20	26	1	2.5	$1 \cdot 10^{-3}$	-96.4	1.25
5	0.4	3.0	30	5	0	10	$8 \cdot 10^{-4}$	-13.2	-0.62

uniform outflow with the same discharge over the right, outer boundary. Based on the Turner angle, a system with double-diffusive convection is expected to build up in Case 3, whereas a gravitationally unstable system is expected to develop in Case 4.

The quantitative validation is based on an analytical solution for the radial expansion of a layer of dense water around a central inflow under laminar flow conditions (Case 5; Table 1). The interface expansion is described by its increasing interface radius r_{int} over time. When the inflow is colder and more saline than the overlying water body, the developing layer has different growth rates for the salinity and temperature interface (Figure 4). This is a consequence of the molecular heat diffusion, which is approximately 100 times larger than the diffusion of salt. In laminar flow conditions, molecular diffusion is the main driver of heat and salt exchange in stable layered systems.

In this quantitative case study, the central inflow has an outer radius of 0.2 m. To allow a slow development of the bottom layer, the inflow is placed slightly deeper compared to the rest of the bottom, and the inflow velocity linearly increases over the first 20 minutes. Like Case 3 and 4, the discharge over the right outflow boundary is set equal to the inflow discharge:

$$Q_{out} = Q_{in} = w_{in} \cdot A_{in} \tag{22}$$

To derive the growth rates of the temperature and salinity interfaces, we consider the similarity solution of the heat equation for a fixed boundary concentration (Bergman et al., 2011):

$$c(x,t) = c_{in} + \triangle c \cdot \mathrm{erfc}\left(\frac{x}{\sqrt{4 \cdot D \cdot t}}\right) \tag{23}$$

where x is the distance from the interface. $\triangle c = c_0 - c_{in}$ is the difference in concentrations (salinity or temperature) between the upper water body, represented by its initial concentration, and the

Geosci. Model Dev. Discuss., doi:10.5194/gmd-2016-176, 2016
Manuscript under review for journal Geosci. Model Dev.
Published: 13 September 2016

Geoscientific Model Development Discussions
Open Access
EGU

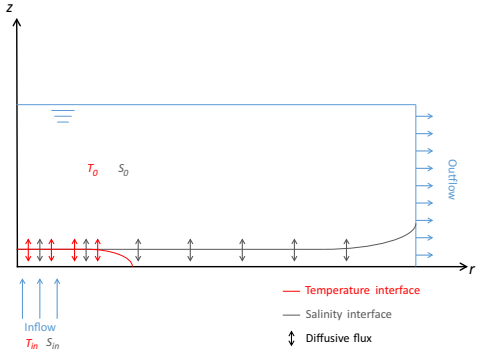

Figure 4. Conceptualization of the quantitative validation (Case 5), with locations of the salinity and temperature interfaces at a certain time after the start of a central inflow. The inflow is colder and more saline than the overlying water body.

inflow. The total mass M that has crossed the interface is found by integration of Equation 23 over $x = 0 \rightarrow \infty$, and multiplication the growing interface surface A_{int}:

$$M(t) = A_{int} \cdot \int_0^\infty (c - c_{in})\, dx = A_{int} \cdot \Delta c \cdot \int_0^\infty \operatorname{erfc}\left(\frac{x}{\sqrt{4 \cdot D \cdot t}}\right) dx = A_{int} \cdot \Delta c \cdot \frac{\sqrt{4 \cdot D \cdot t}}{\pi} \tag{24}$$

Derivation over time results in the time dependent mass flux over the interface:

$$\Phi_{int}(t) = \frac{dM}{dt} = \triangle c \cdot \sqrt{\frac{D \cdot t}{\pi}} \cdot \left(2 \cdot \frac{dA_{int}}{dt} + \frac{A_{int}}{t}\right) \tag{25}$$

With $A_{int} = \pi r_{int}^2$, and assuming that the interface surface increases linearly with time at a constant inflow, we can rewrite:

$$r_{int}(t) = \sqrt{\frac{\Phi_{int}}{3 \cdot \triangle c} \cdot \sqrt{\frac{t}{D \cdot \pi}}} \tag{26}$$

We assume that no mass is stored in the lower layer. Consequently, the mass flux that crosses the interface is equal to the net mass flux into the domain $\Phi_{in} - \Phi_{out} \approx w_{in} \cdot A_{in} \cdot (c_{in} - c_0)$:

$$r_{int}(t) = \sqrt{\frac{w_{in} \cdot A_{in}}{3} \cdot \sqrt{\frac{t}{D \cdot \pi}}} \tag{27}$$

This equation can be used to validate the interface growth of both the salinity and temperature interface in the case of laminar flow.

In all the case studies, we applied a time step of 2 ms and a horizontal mesh size of 5 mm in radial direction. The vertical mesh size in Case 1 and 2 was set uniformly to 10 mm. In the Cases 3 until

Geosci. Model Dev. Discuss., doi:10.5194/gmd-2016-176, 2016
Manuscript under review for journal Geosci. Model Dev.
Published: 13 September 2016

Geoscientific Model Development Discussions
Open Access
EGU

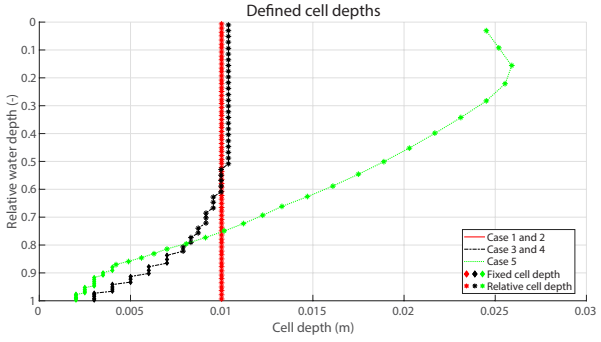

Figure 5. Defined cell depths for the Cases 1 to 5. For plotting reasons, the vertical axis displays the depth from the water surface relative to the local water depth. The cell depths that are defined relative to the local water depth (*) are displayed for the average water depth in each case study.

5, the vertical mesh size varied over depth. Because the processes of most interest occurred near the bottom, the mesh size was decreasing towards the bottom (Figure 5).

3 Results and discussion

The performance of the numerical framework was tested in several case studies subject to double-diffusive processes. The numerical results of these case studies and the extended SWASH code are presented in Hilgersom et al. (2016).

3.1 Case 1 and 2: Salt-fingers

The temperature and salinity gradients in the Cases 1 and 2 yield a theoretical onset of salt-fingers, with respective Turner angles of 71.2^{o} and 85.0^{o}. The numerical results confirm that salt-fingers are formed over the interface (Figure 6). Based on the difference in density ratios, the salt-fingers in Case 2 are hypothesized to transport more salt and heat. Figure 7 shows an interface rise of about 0.02 m in Case 1 and 0.09 m in Case 2 over a numerical model run of 1.5 hours. Given the system of closed boundaries, we therefore find a significantly larger transport over the interface in Case 2.

The effective transport of heat and salt over an interface while maintaining a sharp interface is a clear property of double-diffusive salt-fingers (Turner, 1965). Care should be taken that these salt-fingers are calculated in a 2-D radial grid. Yoshida and Nagashima (2003) pointed out that there is still a lack of knowledge about the 2-D and 3-D structures of salt-fingers and its implications for the interpretation of 2-D numerical results.

Geosci. Model Dev. Discuss., doi:10.5194/gmd-2016-176, 2016
Manuscript under review for journal Geosci. Model Dev.
Published: 13 September 2016

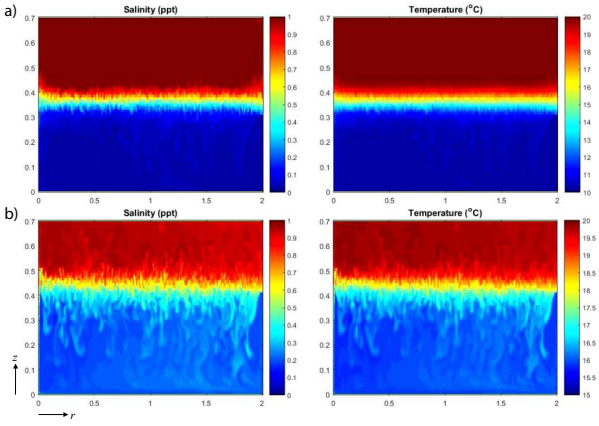

Figure 6. Salt-fingering in a layered system with a warm and saline water on top of a cold and fresh layer (t = 4500 s since the start), with density ratios of a) $R_\rho = 2.04$ (Case 1), and b) $R_\rho = 1.19$ (Case 2).

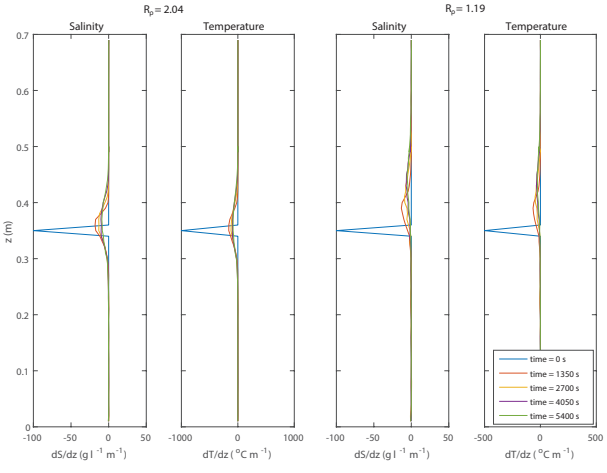

Figure 7. Interface positioning over time, displayed by the derivatives $\partial S/\partial z$ and $\partial T/\partial z$ of the salinity and temperature profiles, for the density ratios $R_\rho = 2.04$ (Case 1) and $R_\rho = 1.19$ (Case 2).

Geosci. Model Dev. Discuss., doi:10.5194/gmd-2016-176, 2016
Manuscript under review for journal Geosci. Model Dev.
Published: 13 September 2016

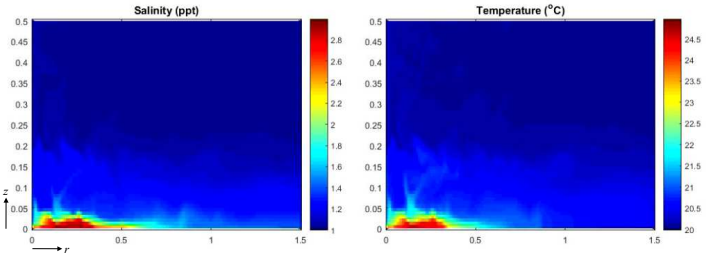

Figure 8. Double-diffusive layering (Case 3) with cold and fresh water on top of a warm and saline inflow ($t = 5400$ s since the start).

3.2 Case 3: Double-diffusive convection

The temperature and salinity gradients in Case 3 yield the onset of double-diffusive convection. Like Case 1 and 2, a sharp interface develops over which salt and heat is transported by diffusion. Figure 8 confirms the development of a salt-heat interface and a convective layer above the boil. Other convective cells further transport the salt and heat above the interface. Figure 8 shows that already a considerable amount of heat and salt was conveyed to the upper layer over the first 1.5 hours. The lower convective layer slowly builds up, and local eddies clearly counteract the development when the lower convective layer is still thin.

3.3 Case 4: Gravitationally unstable system

Compared to Case 3, a slightly altered inflow temperature and salinity in Case 4 theoretically makes the developing layer gravitationally unstable (Table 1). In other words, the water body itself is denser than the inflowing water, which consequently flows upwards. The numerical results confirm the onset of a central buoyant flow above the inflow (Figure 9).

Interestingly, plumes develop from the upward flow. Downward plumes are also visible below the floating warm and saline water. Like the salt-fingers in Case 1 and 2, where warm and saline water also overlaid cold and fresh water, this is a mechanism to dissipate the heat and salt gradients.

3.4 Case 5: Radial expansion of a dense water layer

The analytical solution for the radial expansion of inflowing cold and saline water (Equation 27) holds for a situation with laminar flow. Given the geometric properties of the conceptualized situation and the initially very thin layer of dense water, it is difficult to define the inflow properties so that the flow near the inflow is immediately laminar. For the selected inflow parameters (Table 1), laminarisation of the flow appears to occur after approximately 6000 s (Figure 10). From that moment, the numerical results show significant differences between the salinity and temperature in-

Geosci. Model Dev. Discuss., doi:10.5194/gmd-2016-176, 2016
Manuscript under review for journal Geosci. Model Dev.
Published: 13 September 2016

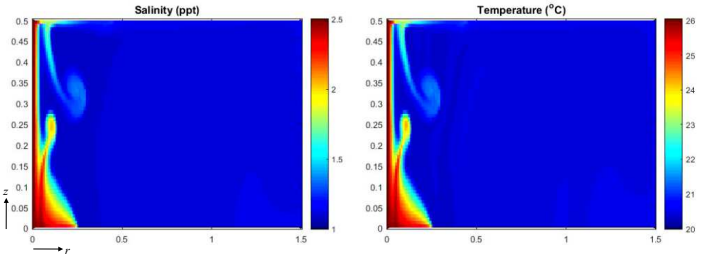

Figure 9. Unstable system (Case 4) with denser cold and fresh water on top of a warm and saline inflow ($t = 1500$ s since the start). The inflowing water flows upward through the centre, independent of the inflow velocity.

terface growth. The analytical results are therefore shifted in time to match the interface radii with the numerical results at the moment that the flow becomes laminar.

Accounting for a purely molecular diffusion, the numerical results show a fair agreement with the analytical results. As we found some small occasional eddies occurring after t = 6000 s, we also plotted results analytical results assuming the diffusivity was on average for 0.5 % influenced by turbulent diffusion. Here, the turbulent diffusion was calculated from a kinematic viscosity $\nu = 10^{-6}$ $\mathrm{m^2 s^{-1}}$ by applying the Prandtl-Schmidt number. The assumption of a slight influence of turbulence diffusion shows a better agreement with the numerical results.

One critical note here is the sensitivity of the interface growth to the definition of the interface location. We defined the interface location at the position of 35 % of the step change between the inflow concentration (T_{in} and S_{in}) and the concentration of the water body (T_0 and S_0), because this matches our visual interpretation of the interface in the numerical results. However, selecting the interface at a larger percentage of the step change significantly increases the growth, and makes the numerical and analytical results incomparable.

4 Conclusions

This study shows the successful derivation of an axisymmetric framework for a hydrodynamic model incorporating salt and heat transport. This model setup allows to efficiently calculate salt and heat transport whenever a situation is modelled that can be approximated by axisymmetry around a central location. The quasi 3-D grid description demands approximately the same execution time as a 2-DV description with the same dense mesh, and therefore avoids the need to solve the equations over a dense mesh in the third spatial dimension.

The derived numerical framework is presented as a Cartesian 2-DV description with few additional terms and width compensation factors. Our implementation of these terms in the non-hydrostatic

Geosci. Model Dev. Discuss., doi:10.5194/gmd-2016-176, 2016
Manuscript under review for journal Geosci. Model Dev.
Published: 13 September 2016

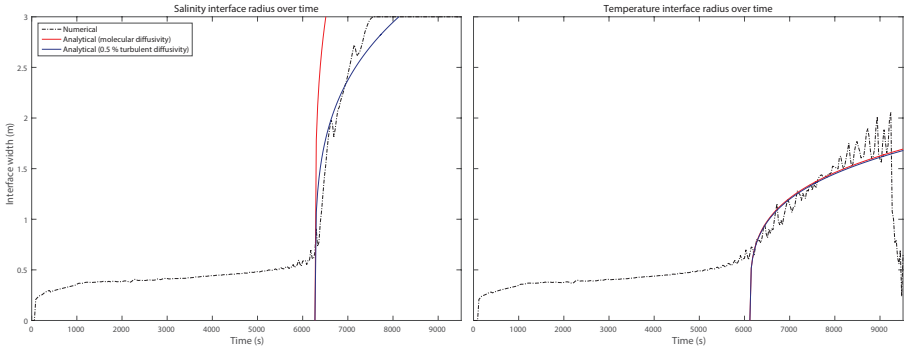

Figure 10. Evolution of the interface between a warm and fresh water body and a bottom cold and saline layer developing form a central inflow. After $t = 6000$ s, the flow in the numerical results becomes laminar and differences between the temperature and salinity interface growth become visible. Analytical results are plotted for the assumptions of completely molecular diffusion (red), and for diffusivities that are for 0.5 % influenced by turbulent diffusion (blue).

SWASH model demonstrates the opportunity to easily expand a 2-DV model towards the presented quasi 3-D model.

For our purpose of studying double-diffusive systems, the SWASH model was further extended with new density and diffusivity modules. The case studies demonstrate explainable behaviour for density and diffusivity driven flow. The formation of convective layers and salt-fingers are in accordance with the theory of double-diffusivity. A quantitative validation method was presented to evaluate the model's performance for a cold and saline inflow developing a dense water layer near the bottom. For laminar flow conditions, the numerical model showed a similar radial expansion of the bottom layer as expected from analytical results.

Data availability

The model data for the five case studies and the extended SWASH code are accessible on doi:10.4121/uuid:c0dce972-5a04-476f-8f3f-4ac34f40da1b (Hilgersom et al., 2016).

Geosci. Model Dev. Discuss., doi:10.5194/gmd-2016-176, 2016
Manuscript under review for journal Geosci. Model Dev.
Published: 13 September 2016

Geoscientific Model Development Discussions
Open Access
EGU

Appendix A: Cell depth integration with the Leibniz integral rule

When the continuity, momentum and transport equations are integrated over the cell depth, the Leibniz integral rule is applied to the time derivatives and the horizontal spatial derivatives. Here, we show the cell depth integration of $\frac{\partial u}{\partial t}$ and $\frac{\partial uu}{\partial r}$:

$$\int_{z_{k-\frac{1}{2}}}^{z_{k+\frac{1}{2}}} \frac{\partial u}{\partial t} dz = \frac{\partial u_k h_k}{\partial t} - u \frac{\partial z}{\partial t}\bigg|_{z_{k-\frac{1}{2}}}^{z_{k+\frac{1}{2}}} \tag{A1}$$

$$\int_{z_{k-\frac{1}{2}}}^{z_{k+\frac{1}{2}}} \frac{\partial uu}{\partial r} dz = \frac{\partial u_k u_k h_k}{\partial r} - u\hat{u} \frac{\partial z}{\partial r}\bigg|_{z_{k-\frac{1}{2}}}^{z_{k+\frac{1}{2}}} \tag{A2}$$

The derivatives $\frac{\partial ur}{\partial r}$, $\frac{\partial w}{\partial t}$, $\frac{\partial uw}{\partial r}$, $\frac{\partial p}{\partial r}$, $\frac{\partial c}{\partial t}$, and $\frac{\partial c}{\partial r}$ in Equations 1, 2, 3, and 7 are integrated in a similar fashion.

Appendix B: Full discretizations

B1 U-momemtum

$$\begin{aligned}
&\frac{u^{n+\theta_u}_{i+\frac{1}{2},k}}{\theta_u \Delta t} + \frac{\overline{\omega^n_{i+\frac{1}{2},k+\frac{1}{2}}}^r \left(\widehat{u}^{n+\theta_u}_{i+\frac{1}{2},k+\frac{1}{2}} - u^{n+\theta_u}_{i+\frac{1}{2},k}\right)}{\overline{h^n_{i+\frac{1}{2},k}}^r} - \frac{\overline{\omega^n_{i+\frac{1}{2},k-\frac{1}{2}}}^r \left(\widehat{u}^{n+\theta_u}_{i+\frac{1}{2},k-\frac{1}{2}} - u^{n+\theta_u}_{i+\frac{1}{2},k}\right)}{\overline{h^n_{i+\frac{1}{2},k}}^r} - \\
&\nu^n_{v;i+\frac{1}{2},k+\frac{1}{2}} \frac{u^{n+\theta_u}_{i+\frac{1}{2},k+1} - u^{n+\theta_u}_{i+\frac{1}{2},k}}{\overline{h^n_{i+\frac{1}{2},k}}^r \overline{h^n_{i+\frac{1}{2},k+\frac{1}{2}}}^{rz}} + \nu^n_{v;i+\frac{1}{2},k-\frac{1}{2}} \frac{u^{n+\theta_u}_{i+\frac{1}{2},k} - u^{n+\theta_u}_{i+\frac{1}{2},k-1}}{\overline{h^n_{i+\frac{1}{2},k}}^r \overline{h^n_{i+\frac{1}{2},k-\frac{1}{2}}}^{rz}} = \frac{u^n_{i+\frac{1}{2},k}}{\theta_u \Delta t} - \\
&\frac{\overline{\phi^n_{i+1,k} \overrightarrow{y_{1;i+1}}}^r \left(\hat{u}^n_{i+1,k} - u^n_{i+\frac{1}{2},k}\right) - \overline{\phi^n_{i,k} \overrightarrow{y_{1;i}}}^r \left(\hat{u}^n_{i,k} - u^n_{i+\frac{1}{2},k}\right)}{\overline{h^n_{i+\frac{1}{2},k}}^r \overline{y_{1;i+\frac{1}{2}}}^r \Delta r_{i+\frac{1}{2}}} + \boxed{\frac{\alpha}{\overline{y_{1;i+\frac{1}{2}}}^r} u^n_{i+\frac{1}{2},k} u^n_{i+\frac{1}{2},k}} - \\
&g \frac{\zeta^{n+\theta_\zeta}_{i+1} - \zeta^{n+\theta_\zeta}_{i}}{\Delta r_{i+\frac{1}{2}}} - \frac{q^n_{i+1,k} h^n_{i+1,k} y_{1;i+1} - q^n_{i,k} h^n_{i,k} y_{1;i}}{\overline{h^n_{i+\frac{1}{2},k}}^r \overline{y_{1;i+\frac{1}{2}}}^r \Delta r_{i+\frac{1}{2}}} + \overline{q^n_{i+\frac{1}{2},k+\frac{1}{2}}}^{rz} \frac{z^n_{i+1,k+\frac{1}{2}} - z^n_{i,k+\frac{1}{2}}}{\overline{h^n_{i+\frac{1}{2},k}}^r \Delta r_{i+\frac{1}{2}}} - \\
&\overline{q^n_{i+\frac{1}{2},k-\frac{1}{2}}}^{rz} \frac{z^n_{i+1,k-\frac{1}{2}} - z^n_{i,k-\frac{1}{2}}}{\overline{h^n_{i+\frac{1}{2},k}}^r \Delta r_{i+\frac{1}{2}}} + \boxed{\frac{\alpha \overline{q^n_{i+\frac{1}{2},k}}^r}{\overline{y_{1;i+\frac{1}{2}}}^r}} - \frac{g}{\rho_0} \frac{\overline{h^n_{i+\frac{1}{2},k}}^r}{2} \frac{\rho^n_{i+1,k} - \rho^n_{i,k}}{\Delta r_{i+\frac{1}{2}}} - \\
&\frac{g}{\rho_0} \sum_{j=1}^{k-1} \left(\overline{h^n_{i+\frac{1}{2},j}}^r \frac{\rho^n_{i+1,j} - \rho^n_{i,j}}{\Delta r_{i+\frac{1}{2}}} + \left(\overline{\rho^n_{i+\frac{1}{2},j}}^r - \overline{\rho^n_{i+\frac{1}{2},k}}^r\right) \frac{h^n_{i+1,j} - h^n_{i,j}}{\Delta r_{i+\frac{1}{2}}} \right) + \\
&\frac{\nu^n_{h;i+1,k} y_{1;i+1} h^n_{i+1,k}}{\overline{h^n_{i+\frac{1}{2},k}}^r \overline{y_{1;i+\frac{1}{2}}}^r \Delta r_{i+\frac{1}{2}}} \frac{u^n_{i+\frac{3}{2},k} - u^n_{i+\frac{1}{2},k}}{\Delta r_{i+1}} - \\
&\frac{\nu^n_{h;i,k} y_{1;i} h^n_{i,k}}{\overline{h^n_{i+\frac{1}{2},k}}^r \overline{y_{1;i+\frac{1}{2}}}^r \Delta r_{i+\frac{1}{2}}} \frac{u^n_{i+\frac{1}{2},k} - u^n_{i-\frac{1}{2},k}}{\Delta r_i} - \boxed{\frac{\alpha}{\overline{y_{1;i+\frac{1}{2}}}^r} u^n_{i+\frac{1}{2},k} \frac{\overline{\nu^n_{h;i+\frac{1}{2},k}}^r}{r_{i+\frac{1}{2}}}}
\end{aligned} \tag{B1}$$

Geosci. Model Dev. Discuss., doi:10.5194/gmd-2016-176, 2016
Manuscript under review for journal Geosci. Model Dev.
Published: 13 September 2016

Geoscientific Model Development Discussions
Open Access
EGU

B2 W-momemtum

$$\frac{w^{n+\theta_w}_{i,k+\frac{1}{2}}}{\theta_w\Delta t}+\frac{\overline{\omega^n_{i,k+1}}^{z}\left(\hat{w}^{n+\theta_w}_{i,k+1}-w^{n+\theta_w}_{i,k+\frac{1}{2}}\right)}{\overline{h^n_{i,k+\frac{1}{2}}}^{z}}-\frac{\overline{\omega^n_{i,k}}^{z}\left(\hat{w}^{n+\theta_w}_{i,k}-w^{n+\theta_w}_{i,k+\frac{1}{2}}\right)}{\overline{h^n_{i,k+\frac{1}{2}}}^{z}}$$
$$-\nu^n_{v;i,k+1}\frac{w^{n+\theta_w}_{i,k+\frac{3}{2}}-w^{n+\theta_w}_{i,k+\frac{1}{2}}}{\overline{h^n_{i,k+\frac{1}{2}}}^{z}h^n_{i,k+1}}+\nu^n_{v;i,k}\frac{w^{n+\theta_w}_{i,k+\frac{1}{2}}-w^{n+\theta_w}_{i,k-\frac{1}{2}}}{\overline{h^n_{i,k+\frac{1}{2}}}^{z}h^n_{i,k}}=\frac{w^n_{i,k+\frac{1}{2}}}{\theta_w\Delta t}$$
$$-\frac{\overline{\phi^n_{i+\frac{1}{2},k+\frac{1}{2}}}^{z}\overrightarrow{y_{1;i+\frac{1}{2}}}\left(\hat{w}^n_{i+\frac{1}{2},k+\frac{1}{2}}-w^n_{i,k+\frac{1}{2}}\right)-\overline{\phi^n_{i-\frac{1}{2},k+\frac{1}{2}}}^{z}\overrightarrow{y_{1;i-\frac{1}{2}}}\left(\hat{w}^n_{i-\frac{1}{2},k+\frac{1}{2}}-w^n_{i,k+\frac{1}{2}}\right)}{\overline{h^n_{i,k+\frac{1}{2}}}^{z}y_{1;i}\Delta r_i}$$
$$+\boxed{\frac{\alpha}{y_{1;i}}\frac{\overline{\phi^n_{i,k+\frac{1}{2}}}^{rz}}{\overline{h^n_{i,k+\frac{1}{2}}}^{z}}w^n_{i,k+\frac{1}{2}}}-\frac{q^n_{i,k+1}}{\overline{h^n_{i,k+\frac{1}{2}}}^{z}}+\frac{q^n_{i,k}}{\overline{h^n_{i,k+\frac{1}{2}}}^{z}}+\frac{\nu^n_{h;i+\frac{1}{2},k+\frac{1}{2}}\overline{y_{1;i+\frac{1}{2}}}^{r}\overline{h^n_{i-\frac{1}{2},k+\frac{1}{2}}}^{rz}}{\overline{h^n_{i,k+\frac{1}{2}}}^{z}y_{1;i}\Delta r_i}\frac{w^n_{i+1,k+\frac{1}{2}}-w^n_{i,k+\frac{1}{2}}}{\Delta r_{i+\frac{1}{2}}}$$
$$-\frac{\nu^n_{h;i-\frac{1}{2},k+\frac{1}{2}}\overline{y_{1;i-\frac{1}{2}}}^{r}\overline{h^n_{i-\frac{1}{2},k+\frac{1}{2}}}^{rz}}{\overline{h^n_{i,k+\frac{1}{2}}}^{z}y_{1;i}\Delta r_i}\frac{w^n_{i,k+\frac{1}{2}}-w^n_{i-1,k+\frac{1}{2}}}{\Delta r_{i-\frac{1}{2}}} \tag{B2}$$

B3 Transport equation

$$\frac{c^{n+1}_{i,k}}{\Delta t}+\frac{\omega^{n+1}_{i,k+\frac{1}{2}}\hat{c}^{n+1}_{i,k+\frac{1}{2}}}{h^{n+1}_{i,k}}-\frac{\omega^{n+1}_{i,k-\frac{1}{2}}\hat{c}^{n+1}_{i,k-\frac{1}{2}}}{h^{n+1}_{i,k}}-\frac{D_{v;i,k+\frac{1}{2}}}{h^{n+1}_{i,k}}\frac{c^{n+1}_{i,k+1}-c^{n+1}_{i,k}}{\overline{h^{n+1}_{i,k+\frac{1}{2}}}^{z}}+$$
$$\frac{D_{v;i,k-\frac{1}{2}}}{h^{n+1}_{i,k}}\frac{c^{n+1}_{i,k}-c^{n+1}_{i,k-1}}{\overline{h^{n+1}_{i,k-\frac{1}{2}}}^{z}}=\frac{c^n_{i,k}h^n_{i,k}}{\Delta t h^{n+1}_{i,k}}-\frac{\phi^n_{i+\frac{1}{2},k}\overrightarrow{y_{1;i+\frac{1}{2}}}\hat{c}^n_{i+\frac{1}{2},k}}{y_{1;i}h^{n+1}_{i,k}\Delta r}+\frac{\phi^n_{i-\frac{1}{2},k}\overrightarrow{y_{1;i-\frac{1}{2}}}\hat{c}^n_{i-\frac{1}{2},k}}{y_{1;i}h^{n+1}_{i,k}\Delta r}+$$
$$\frac{D_{h;i+\frac{1}{2},k}\overline{y_{1;i+\frac{1}{2}}}^{r}\overline{h^n_{i+\frac{1}{2},k}}^{r}}{y_{1;i}h^{n+1}_{i,k}\Delta r}\frac{c^n_{i+1,k}-c^n_{i,k}}{\Delta r}-\frac{D_{h;i-\frac{1}{2},k}\overline{y_{1;i-\frac{1}{2}}}^{r}\overline{h^n_{i-\frac{1}{2},k}}^{r}}{y_{1;i}h^{n+1}_{i,k}\Delta r}\frac{c^n_{i,k}-c^n_{i-1,k}}{\Delta r}-$$
$$\frac{D_{h;i+\frac{1}{2},k}\overline{y_{1;i+\frac{1}{2}}}^{r}\overline{h^n_{i+\frac{1}{2},k}}^{r}}{y_{1;i}h^{n+1}_{i,k}\Delta r}\frac{\overline{c^n_{i+\frac{1}{2},k+1}}^{r}-\overline{c^n_{i+\frac{1}{2},k-1}}^{r}}{\overline{h^n_{i+\frac{1}{2},k+\frac{1}{2}}}^{rz}+\overline{h^n_{i+\frac{1}{2},k-\frac{1}{2}}}^{rz}}\frac{\overline{z^n_{i+1,k}}^{z}-\overline{z^n_{i,k}}^{z}}{\Delta r}+$$
$$\frac{D_{h;i-\frac{1}{2},k}\overline{y_{1;i-\frac{1}{2}}}^{r}\overline{h^n_{i-\frac{1}{2},k}}^{r}}{y_{1;i}h^{n+1}_{i,k}\Delta r}\frac{\overline{c^n_{i-\frac{1}{2},k+1}}^{r}-\overline{c^n_{i-\frac{1}{2},k-1}}^{r}}{\overline{h^n_{i-\frac{1}{2},k+\frac{1}{2}}}^{rz}+\overline{h^n_{i-\frac{1}{2},k-\frac{1}{2}}}^{rz}}\frac{\overline{z^n_{i,k}}^{z}-\overline{z^n_{i-1,k}}^{z}}{\Delta r}-$$
$$\frac{D_{h;i,k+\frac{1}{2}}}{h^{n+1}_{i,k}}\frac{z^n_{i+1,k+\frac{1}{2}}-z^n_{i-1,k+\frac{1}{2}}}{2\Delta r}\frac{\overline{c^n_{i+1,k+\frac{1}{2}}}^{z}-\overline{c^n_{i-1,k+\frac{1}{2}}}^{z}}{2\Delta r}+$$
$$\frac{D_{h;i,k+\frac{1}{2}}}{h^{n+1}_{i,k}}\left(\frac{z^n_{i+1,k+\frac{1}{2}}-z^n_{i-1,k+\frac{1}{2}}}{2\Delta r}\right)^2\frac{c^n_{i,k+1}-c^n_{i,k}}{\overline{h^n_{i,k+\frac{1}{2}}}^{z}}-$$
$$\frac{D_{h;i,k-\frac{1}{2}}}{h^{n+1}_{i,k}}\left(\frac{z^n_{i+1,k-\frac{1}{2}}-z^n_{i-1,k-\frac{1}{2}}}{2\Delta r}\right)^2\frac{c^n_{i,k}-c^n_{i,k-1}}{\overline{h^n_{i,k-\frac{1}{2}}}^{z}} \tag{B3}$$

Acknowledgements. This project has been funded by The Netherlands Organisation for Scientific Research (NWO), project number 842.00.004.

Geosci. Model Dev. Discuss., doi:10.5194/gmd-2016-176, 2016
Manuscript under review for journal Geosci. Model Dev.
Published: 13 September 2016

References

Arnon, A., Lensky, N. G., and Selker, J. S.: High-resolution temperature sensing in the Dead Sea using fiber optics, Water Resour. Res., 50, 1756–1772, doi:10.1002/2013WR014935, 2014.

Batchelor, G.: An introduction to fluid dynamics, Cambridge Univ. Pr., 1967.

Bennett, G., Reilly, T., and Hill, M.: Technical training notes in ground-water hydrology: radial flow to a well, Tech. rep., US Geological Survey; Books and Open-File Reports, 1990.

Bergman, T. L., Incropera, F. P., and Lavine, A. S.: Fundamentals of heat and mass transfer, John Wiley & Sons, 2011.

Berthold, S. and Börner, F.: Detection of free vertical convection and double-diffusion in groundwater monitoring wells with geophysical borehole measurements, Environ. Geol., 54, 1547–1566, doi:10.1007/s00254-007-0936-y, 2008.

Casulli, V. and Cheng, R. T.: Semi-implicit finite difference methods for three-dimensional shallow water flow, Int. J. Numer. Meth. Fl., 15, 629–648, doi:10.1002/fld.1650150602, 1992.

Casulli, V. and Stelling, G.: Numerical simulation of 3D quasi-hydrostatic, free-surface flows, J. Hydraul. Eng.-ASCE, 124, 678–686, 1998.

Cathcart, T. P. and Wheaton, F. W.: Modeling temperature distribution in freshwater ponds, Aquacult. Eng., 6, 237 – 257, doi:10.1016/0144-8609(87)90021-5, 1987.

De Louw, P., Vandenbohede, A., Werner, A., and Oude Essink, G.: Natural saltwater upconing by preferential groundwater discharge through boils, J. Hydrol., 490, 74 – 87, doi:10.1016/j.jhydrol.2013.03.025, 2013.

Dias, J. and Lopes, J.: Implementation and assessment of hydrodynamic, salt and heat transport models: The case of Ria de Aveiro Lagoon (Portugal), Environ. Modell. Softw., 21, 1 – 15, doi:10.1016/j.envsoft.2004.09.002, 2006.

Eckart, C. H.: The equation of state of water and sea water at low temperatures and pressures, Part 2 of Properties of water, American Journal of Science, 256, 225–240, 1958.

Fringer, O., Armfield, S., and Street, R.: Reducing numerical diffusion in interfacial gravity wave simulations, Int. J. Numer. Meth. Fl., 49, 301–329, 2005.

Galletti, C., Parente, A., and Tognotti, L.: Numerical and experimental investigation of a mild combustion burner, Combust. Flame, 151, 649–664, 2007.

Giestas, M., Pina, H. L., Milhazes, J. P., and Tavares, C.: Solar pond modeling with density and viscosity dependent on temperature and salinity, Int. J. Heat Mass Tran., 52, 2849 – 2857, doi:10.1016/j.ijheatmasstransfer.2009.01.003, 2009.

Hilgersom, K., Zijlema, M., and van de Giesen, N.: An axisymmetric hydrodynamical model: model code and data, TU Delft, doi:10.4121/uuid:c0dce972-5a04-476f-8f3f-4ac34f40da1b, 2016.

Hirsch, C.: Numerical Computation of Internal and External Flows, Wiley, Chichester, 1988.

Huppert, H. E. and Turner, J.: Double-diffusive convection, J. Fluid Mech., 106, 299–329, 1981.

Kelley, D. E., Fernando, H. J. S., Gargett, A. E., Tanny, J., and Özsoy, E.: The diffusive regime of double-diffusive convection, Prog. Oceanogr., 56, 461 – 481, doi:10.1016/S0079-6611(03)00026-0, 2003.

Kimura, S., Smyth, W., and Kunze, E.: Turbulence in a sheared, salt-fingering-favorable environment: Anisotropy and effective diffusivities, J. Phys. Oceanogr., 41, 1144–1159, 2011.

Geosci. Model Dev. Discuss., doi:10.5194/gmd-2016-176, 2016
Manuscript under review for journal Geosci. Model Dev.
Published: 13 September 2016

Kunze, E.: A review of oceanic salt-fingering theory, Prog. Oceanogr., 56, 399 – 417, doi:10.1016/S0079-6611(03)00027-2, 2003.

Langevin, C. D.: Modeling Axisymmetric Flow and Transport, Ground Water, 46, 579–590, doi:10.1111/j.1745-6584.2008.00445.x, 2008.

Launder, B. and Spalding, D.: The numerical computation of turbulent flows, Comput. Method Appl. M., 3, 269 – 289, doi:10.1016/0045-7825(74)90029-2, 1974.

Menguc, M. and Viskanta, R.: Radiative transfer in axisymmetric, finite cylindrical enclosures, J. Heat Transf., 108, 271–276, 1986.

Reilly, T. E. and Harbaugh, A. W.: Simulation of Cylindrical Flow to a Well Using the US Geological Survey Modular Finite-Difference Ground-Water Flow Model, Ground Water, 31, 489–494, 1993.

Ruddick, B.: A practical indicator of the stability of the water column to double-diffusive activity, Deep-Sea Res. Pt. I, 30, 1105–1107, 1983.

Ruddick, B. and Gargett, A. E.: Oceanic double-infusion: introduction, Prog. Oceanogr., 56, 381 – 393, doi:10.1016/S0079-6611(03)00024-7, 2003.

Schmid, M., Lorke, A., Wüest, A., Halbwachs, M., and Tanyileke, G.: Development and sensitivity analysis of a model for assessing stratification and safety of Lake Nyos during artificial degassing, Ocean Dynam., 53, 288–301, 2003.

Schmid, M., Lorke, A., Dinkel, C., Tanyileke, G., and Wüest, A.: Double-diffusive convection in Lake Nyos, Cameroon, Deep-Sea Res. Pt. I, 51, 1097 – 1111, doi:10.1016/j.dsr.2004.02.010, 2004.

Schubert, F., Peiffer, A., Köhler, B., and Sanderson, T.: The elastodynamic finite integration technique for waves in cylindrical geometries, J. Acoust. Soc. Am., 104, 2604–2614, 1998.

Shima, E., Matsuda, T., Takeda, H., and Sawada, K.: Hydrodynamic calculations of axisymmetric accretion flow, Mon. Not. R. Astron. Soc., 217, 367–386, doi:10.1093/mnras/217.2.367, 1985.

Stern, M. E.: Lateral mixing of water masses, Deep-Sea Res., 14, 747 – 753, doi:10.1016/S0011-7471(67)80011-1, 1967.

Stommel, H. and Fedorov, K.: Small scale structure in temperature and salinity near Timor and Mindanao, Tellus A, 19, 1967.

Stommel, H., Arons, A., and Blanchard, D.: An oceanographical curiosity: the perpetual salt fountain, Deep-Sea Res., 3, 152–153, 1956.

Suárez, F., Tyler, S., and Childress, A.: A fully coupled, transient double-diffusive convective model for salt-gradient solar ponds, Int. J. Heat Mass Tran., 53, 1718–1730, doi:10.1016/j.ijheatmasstransfer.2010.01.017, 2010.

Suárez, F., Ruskowitz, J. A., Childress, A. E., and Tyler, S. W.: Understanding the expected performance of large-scale solar ponds from laboratory-scale observations and numerical modeling, Appl. Energ., 117, 1 – 10, doi:10.1016/j.apenergy.2013.12.005, 2014.

SWASH source code: http://swash.sourceforge.net/, accessed on: 30 May 2016, http://swash.sourceforge.net/, 2010.

Traxler, A., Stellmach, S., Garaud, P., Radko, T., and Brummeln, N.: Dynamics of fingering convection. Part 1 Small-scale fluxes and large-scale instabilities, J. Fluid Mech., 677, 530–553, doi:10.1017/jfm.2011.98, 2011.

Geosci. Model Dev. Discuss., doi:10.5194/gmd-2016-176, 2016
Manuscript under review for journal Geosci. Model Dev.
Published: 13 September 2016

Turner, J.: The coupled turbulent transports of salt and and heat across a sharp density interface, Int. J. Heat Mass Tran., 8, 759 – 760, IN3–IN4, 761–767, doi:10.1016/0017-9310(65)90022-0, 1965.

Unesco: Tenth report of the joint panel on oceanographic tables and standards, UNESCO Tech. Paper in Marine Science, 36, 25, 1981.

Vega, L. A.: Ocean Thermal Energy Conversion Primer, Mar. Technol. Soc. J., 36, 25–35, doi:10.4031/002533202787908626, 2002.

Washburn, E. W. and West, C. J.: International Critical Tables of Numerical Data, Physics, Chemistry and Technology: Vol. 1-7, McGraw-Hill, 1933.

Wright, D. G.: An Equation of State for Use in Ocean Models: Eckart's Formula Revisited, J. Atmos. Oceanic Technol., 14, 735–740, doi:10.1175/1520-0426(1997)014<0735:AEOSFU>2.0.CO;2, 1997.

Yoshida, J. and Nagashima, H.: Numerical experiments on salt-finger convection, Prog. Oceanogr., 56, 435 – 459, doi:10.1016/S0079-6611(03)00032-6, 2003.

Zijlema, M. and Stelling, G.: Efficient computation of surf zone waves using the nonlinear shallow water equations with non-hydrostatic pressure, Coast. Eng., 55, 780–790, 2008.

Zijlema, M. and Stelling, G. S.: Further experiences with computing non-hydrostatic free-surface flows involving water waves, Int. J. Numer. Meth. Fl., 48, 169–197, doi:10.1002/fld.821, 2005.

Zijlema, M., Stelling, G., and Smit, P.: SWASH: An operational public domain code for simulating wave fields and rapidly varied flows in coastal waters, Coast. Eng., 58, 992 – 1012, doi:10.1016/j.coastaleng.2011.05.015, 2011.